



HAL
open science

Mechanical behavior and microstructure evolution during deformation of AA7075-T651

Biswajit Dalai, Marie Anna Moretti, Paul Åkerström, Corinne Arvieu, Dimitri Jacquin, Lars-Erik Lindgren, Marie Moretti

► **To cite this version:**

Biswajit Dalai, Marie Anna Moretti, Paul Åkerström, Corinne Arvieu, Dimitri Jacquin, et al.. Mechanical behavior and microstructure evolution during deformation of AA7075-T651. *Materials Science and Engineering: A*, 2021, 822, pp.141615. 10.1016/j.msea.2021.141615 . hal-03613054

HAL Id: hal-03613054

<https://hal.inrae.fr/hal-03613054>

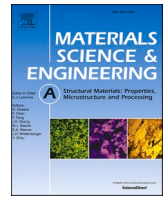
Submitted on 18 Mar 2022

HAL is a multi-disciplinary open access archive for the deposit and dissemination of scientific research documents, whether they are published or not. The documents may come from teaching and research institutions in France or abroad, or from public or private research centers.

L'archive ouverte pluridisciplinaire **HAL**, est destinée au dépôt et à la diffusion de documents scientifiques de niveau recherche, publiés ou non, émanant des établissements d'enseignement et de recherche français ou étrangers, des laboratoires publics ou privés.



Distributed under a Creative Commons Attribution 4.0 International License



Mechanical behavior and microstructure evolution during deformation of AA7075-T651

Biswajit Dalai^{a,*}, Marie Anna Moretti^a, Paul Åkerström^a, Corinne Arvieu^b, Dimitri Jacquin^b, Lars-Erik Lindgren^a

^a Department of Engineering Sciences and Mathematics, Luleå University of Technology, 97187, Luleå, Sweden

^b University of Bordeaux, CNRS, Arts et Métiers Institute of Technology, Bordeaux INP, INRAE, I2M, Bordeaux, 33400, Talence, France

ARTICLE INFO

Keywords:

Aluminum alloys
Characterization
Stress/strain measurements
Electron back-scattered diffraction (EBSD)
Dynamic recrystallization (DRX)

ABSTRACT

In view of developing a physics-based constitutive material model for AA7075-T651, the mechanical behavior and microstructure evolution of the material has been studied through compression tests using Gleeble thermo-mechanical simulator. The tests were performed at wide range of temperatures (room temperature (RT), 100, 200, 300, 400 and 500 °C) with two constant strain rates (0.01 and 1 s⁻¹). The true stress-strain curves depicted an increase in the flow stress with increase in the strain rate and decrease in the deformation temperature, with an exception at RT. The effects of softening mechanisms, such as adiabatic heating, dissolution of precipitates, dynamic recovery (DRV) and dynamic recrystallization (DRX), on the flow stress level, strain rate sensitivity (SRS) and temperature sensitivity over the entire range of temperatures were analyzed. Pertaining to the microstructure analysis, the intermetallic particles present in the initial as-received (AR) material were identified as (Al,Cu)₆(Fe,Cu) and SiO₂ with the help of back-scattered electron (BSE) imaging and energy dispersive X-ray spectroscopy (EDS). The microstructure of the material after the deformation processes were analyzed and compared with that of the AR state using inverse pole figures (IPF), grain orientation spread (GOS) and grain boundary rotation maps generated from electron back-scattered diffraction (EBSD) scans. DRV was observed for deformation at 300 °C, whereas a combination of DRV and incomplete DRX took place for 400 and 500 °C depending on the strain rate. The fraction of recrystallized grains was higher in case of deformation at higher temperature and lower strain rate. Furthermore, the difference in microstructure evolution on different surfaces of the deformed samples as well as at different locations on individual surfaces was also investigated.

1. Introduction

Aluminum alloy 7075 (AA7075) is one of the strongest, heat-treatable, wrought aluminum alloys belonging to the Al-Zn-Mg-Cu family (7xxx series). This material attains its peak strength via precipitation hardening during T6 and T651 heat treatment processes. The T6 heat treatment consists of the following two steps [1,2]:

- (i) *Solution heat treatment (SHT)*: The alloy is heated up and held at high temperature (usually around 460–490 °C) for a suitable period of time causing the dissolution of second phases in the Al matrix to create a single-phase alloy and then quenched rapidly to room temperature (RT), forming a super saturated solid solution (SSSS).

- (ii) *Age-hardening*: Solution heat treated material is artificially aged at 120 °C for 24 h.

T651 temper signifies that the material is first T6 heat treated and then stress relieved by stretching to 0.5–2% [3]. Many researchers have analyzed the effects of temperature and holding time for SHT and age-hardening steps on the final microstructure and mechanical properties of the AA7075 alloy in order to determine the optimized condition for its T6 heat treatment [4–7].

During the aging process of AA7075, finely dispersed MgZn₂ precipitates are formed in the matrix according to the usual sequence followed by Al 7xxx series [8–10]:

SSSS (α-phase) => Guinier-Preston (GP) zone => Metastable MgZn₂ (η') phase => Stable MgZn₂ (η) phase.

* Corresponding author.

E-mail address: biswajit.dalai@ltu.se (B. Dalai).

Table 1
Chemical composition of AA7075-T651 alloy.

| Element | Zn | Mg | Cu | Cr | Fe | Mn | Si | Ti | Al | Ref. |
|----------|---------|---------|-------|-----------|------|------|------|------|-----------|------|
| | 5.1–6.1 | 2.1–2.9 | 1.2–2 | 0.18–0.28 | <0.5 | <0.3 | <0.4 | <0.2 | 87.1–91.4 | [15] |
| Weight % | 5.56 | 2.36 | 1.57 | 0.19 | 0.23 | 0.12 | 0.17 | 0.07 | 89.73 | [55] |
| | 5.26 | 2.72 | 1.41 | 0.16 | 0.08 | 0.06 | 0.1 | 0.07 | 90.13 | EDS |

The metastable η' precipitate is the main constituent strengthening factor in peak-aged (T6 and T651) AA7075 [11–13] due to its existence in abundance and strong pinning effect on dislocations which strengthens the material [4,6]. On account of the extraordinary combination of properties manifested in the T6 condition such as high mechanical strength, light weight, dimensional stability, machinability, good vibration-damping characteristics and specific stiffness, AA7075 is widely used in this temper state for structural applications in aerospace, military and automobile industries, for example, in aircraft fittings, fuse parts, shafts and gears, missile parts, regulating valves, worm gears, sensor and guidance components for flight and satellite systems, etc. [14–16].

The efficiency and life span of these structural components depend on their constituent material properties and mechanical state at the end of the manufacturing processes as well as during the in-service operating conditions. The mechanical state of a component experiencing different conditions of strain rate and thermal gradient is usually predicted by models incorporating the flow behavior and properties of the constituent material. Many researchers have endeavored to simulate the mechanical response of AA7075 during hot deformation with the help of empirical models that are based on fitting the flow stress curves obtained from the mechanical tests to the model equations [17–28]. On the contrary, the literature study so far revealed only a few physics-based models developed for AA7075 alloy which include the actual underlying physical mechanisms such as dynamic recrystallization (DRX), dislocation density evolution, grain growth, dynamic strain aging (DSA), etc. that take place during the deformation and significantly influence the flow stress behavior of the material [29–32]. On that account, the ultimate goal of our project is to develop a physics-based constitutive model for AA7075 peak-aged at T651 temper which can be used in finite element simulation of manufacturing processes such as machining and friction stir welding (FSW) in order to predict the final state of the material.

Developing the model requires both calibrations using experimental flow stress curves and knowledge about the underlying deformation mechanisms and the microstructure evolution. AA7075 alloy in its peak-aged temper has been reported to consist of three types of second phase precipitates: (a) strengthening particles, (b) dispersoids, and (c) intermetallics. Due to their very small size, strengthening particles (2–80 nm [9,11,33–35]) and dispersoids (20–500 nm [9,16,36,37]) are normally identified under transmission electron microscope (TEM), whereas intermetallic particles, which are comparatively larger in size (2–20 μm [4,37,38]), can be observed using scanning electron microscope (SEM) as well. As already mentioned, the strengthening particles are generated during age-hardening process. Dispersoids are formed in the microstructure due to the reaction of Cr with the alloying elements Zn, Mg and Cu during homogenization. They control the grain size and degree of recrystallization (RX) in the alloy by pinning the grain boundaries [16,36,37]. The irregular shaped intermetallic particles are usually created during the manufacturing processes due to the interaction between alloying elements and impurities present in the alloy [37] and they influence the strength and hardness of the material [4,5]. These second phase precipitates play an important role in the evolution of microstructure during the high temperature deformation of AA7075-T651.

Mechanical tests at varied conditions of strain rates and temperatures provide the base for calibration of the model. The flow stress

behavior of AA7075 alloy in its different states has been extensively studied for deformation at RT–580 °C with strain rates ranging between in the order of 10^{-3} s^{-1} and 10 s^{-1} [18–21,25–29,39–50]. Conventionally, the flow stress for the alloy increases with strain rate and decreases with deformation temperature. However, exceptions to this behavior have been observed at quasi-static strain rates (in the order of $10^{-5} - 10^{-4} \text{ s}^{-1}$), where the flow stress increased with increase in temperature from RT to 100 °C [51,52]. Similar exceptional behavior has been detected and attributed to DSA effect when the alloy was first solution heat treated at 300–475 °C and then deformed with $10^{-5} - 10^{-1} \text{ s}^{-1}$ [31,32]. Characteristically, the effect of temperature on the flow stress behavior of the alloy has been observed to be more pronounced than that of the strain rate. Furthermore, the material has been reported to have undergone deformation mechanisms such as lattice-diffusion controlled dislocation climb [19], formation of shear bands via localized plastic deformation [19,20,45], micro cracking at material inhomogeneity [45,48], lubricated flow [39], etc. during compression at $10^{-3} - 10 \text{ s}^{-1}$ strain rates within different temperature ranges. From the microstructure evolution standpoint in case of hot deformation of AA7075 within the above-mentioned strain rates, dynamic recovery (DRV) has been reported to be the governing softening mechanism at high temperatures up to 350 °C [29,41]. Whereas, DRX takes over in case of deformation temperatures between 350 °C and 550 °C via: (a) continuous dynamic recrystallization (CDRX) [30,39,41,43] which, conventionally, is the dominant mechanism for materials having high stacking fault energy (SFE) such as Al alloys, α -iron, titanium and its alloys [53], and (b) geometrical dynamic recrystallization (GDRX) [39,41] which is promoted by initial elongated columnar grain structure generated from one-directional manufacturing processes, such as rolling and extrusion. Even though usually rapid DRV takes place in high SFE materials during high temperature deformation and thereby prevents discontinuous dynamic recrystallization (DDRX) [53], Rokni et al. [39] reported DDRX in AA7075 in case of deformation with low strain rate above the solidus temperature of the material. Compared to the low strain rates discussed above, the literature comprises fewer research works examining the deformation behavior of AA7075 in its different states at higher strain rates in the order of $10^2 - 10^3 \text{ s}^{-1}$ [24,26,27,44,46,50,52,54].

Out of all the studies reported in the previous paragraph about the deformation behavior of AA7075 alloy in its different states, only a few of them are based on the T651 state [46,52,54], which is the material under investigation in the current study. Furthermore, these studies focused on different ranges of temperatures, thereby leaving quite many areas in between with scopes for more investigation, such as flow stress behavior of the alloy at lower deformation temperatures (< 250 °C), sensitivity of the flow stress with respect to strain rate and temperature as well as effects of various softening mechanisms over the entire temperature region ranging from RT to 500 °C, etc., which have been attempted to address to in the current study. More importantly, in spite of all the microstructural features reported in the literature, there is still a lack of better microscopic demonstration through electron back-scattered diffraction (EBSD) analysis pertaining to the effects of temperature, strain rate and sample location on the DRX taking place during the deformation of AA7075-T651, which is crucial in developing a physics-based material model and that is why the primary focus of our current research.

To summarize, our current study deals with the low strain rate deformation and microstructure characterization of AA7075-T651, as a

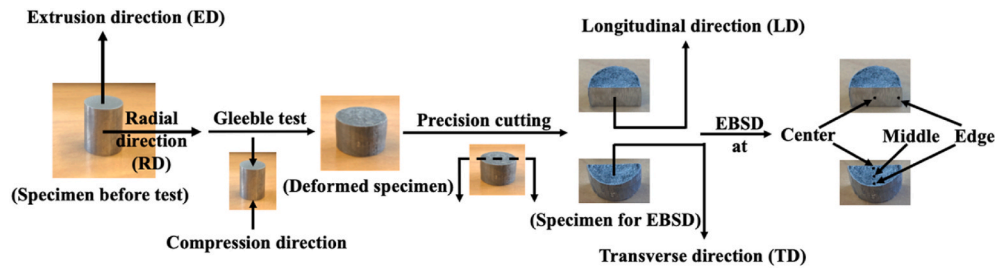


Fig. 1. Graphical representation of a sample before and after deformation, its different surfaces prepared for EBSD scans, and different locations on the surfaces where EBSD scans were taken.

steppingstone to develop a physics-based constitutive model which will, in turn, be implemented in simulation of manufacturing processes for predicting the final state of the material.

2. Experimental details

2.1. Material

In our research, we have used AA7075-T651 alloy provided by Alumeco [55]. The starting material was extruded circular bars of AA7075 alloy which were drawn to 10 mm diameter. Then the round bars were aged to T651 temper condition. Table 1 displays the chemical composition limits for AA7075 alloy recommended by Aerospace Specification Metals Inc. (ASM) [15] and the compositions that we received from Alumeco as well as from energy dispersive X-ray spectroscopy (EDS) analysis. It is to be noted that EDS is best described as “semi-quantitative” in capability [56]. The table shows that the alloy compositions from the manufacturer and the EDS results are consistent with the standard recommendations.

2.2. Mechanical characterization

Mechanical behavior of the AA7075-T651 alloy was studied by performing compression tests at RT ($\sim 23^\circ\text{C}$), 100, 200, 300, 400 and 500°C with two constant strain rates of 0.01 and 1 s^{-1} . The tests were carried out using cylindrical samples with 12.5 mm length and 10 mm diameter inside a Gleeble-3800 thermo-mechanical simulator with compression direction parallel to the extrusion direction of the material. 0.125 mm thick graphite foils with nickel paste were used as lubricant to reduce the friction between the anvils of the machine and the specimens. For deformation at elevated temperatures, the samples were first heated up to the intended deformation temperature at a heating rate of 10°C/s and held for 10 s to ensure a homogeneous temperature distribution throughout the specimen. Then they were compressed up to a true strain of ~ 0.6 with the selected strain rates. The temperature of the specimens was measured using K-type (Chromel-Alumel) thermocouple welded on to the center of the curved surface of the samples. The stress and strains developed in the material were obtained using the measurements from the L-gauge fitted inside the compression chamber of the Gleeble machine. The tests were repeated in order to secure consistent results.

2.3. Microstructural characterization

The as-received (AR) and deformed specimens were sectioned in the middle along a direction parallel to the compression axis. One half of the cut specimens was prepared to observe the microstructure on the surface perpendicular to the compression axis and the other half was prepared for observation on the surface parallel to the compression axis. For simplicity of expression, hereafter, we name these two sample surfaces as transverse direction (TD) and longitudinal direction (LD), respectively. In order to investigate any probable variations in the microstructure at different locations on a deformed specimen, electron back-

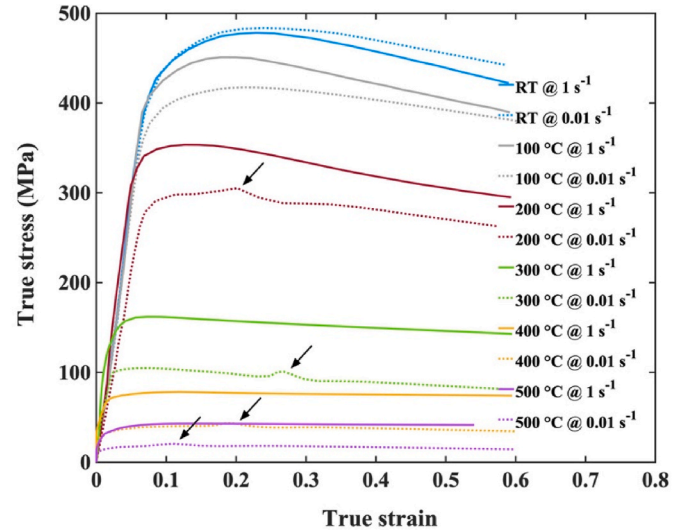


Fig. 2. True stress-strain curves of AA7075-T651 at different temperatures and strain rates. Black arrows indicate humps in the flow stress level.

scattered diffraction (EBSD) images were captured at: (a) the approximate center, (b) towards the edge, and (c) in between center and edge, on the two surfaces of the samples. Fig. 1 portrays a better visual idea about specimen before and after deformation as well as the different sections and locations where the microscopic observations were carried out.

The specimens were mechanically ground with P400 and P1200 grit SiC paper followed by polishing using 3- and $1\text{-}\mu\text{m}$ diamond paste and then with $0.05\text{-}\mu\text{m}$ colloidal silica (OPS) solution. In order to obtain comprehensive EBSD patterns, the samples were electro-polished using a solution of 78 ml perchloric acid (60%), 730 ml ethanol (96%), 100 ml butoxyethanol and 90 ml distilled water. The electro-polishing was conducted at 12–15 V, depending on the surface area, for 10 s.

The polished samples were analyzed using FEI-Nova NNS 450 and JEOL-IT300 SEM in back-scattered electron (BSE) imaging mode for better visualization of the microstructure. The compositions of the matrix and the constituting particles were obtained using EDS scans run at 20 kV using a BRUKER detector. EBSD maps were captured using an EDAX detector in the FEI-SEM with 15 kV beam voltage, $1\text{ }\mu\text{m}$ step size and 200x magnification. The scans were run at a distance of minimum $300\text{ }\mu\text{m}$ inside from the border of the samples in order to avoid the possibility of drifting very close to the border.

Orientation Imaging Microscopy (OIM) software was used to analyze the EBSD images. First of all, a “grain” was defined by setting the grain tolerance angle to 15° , the minimum grains size to 10 pixels and the minimum confidence index (CI) to 0.1. For better presentation of images, the inverse pole figures (IPF) shown in this work do not incorporate the grain definition. However, all other analyses such as grain orientation spread (GOS) and grain boundary rotation maps are

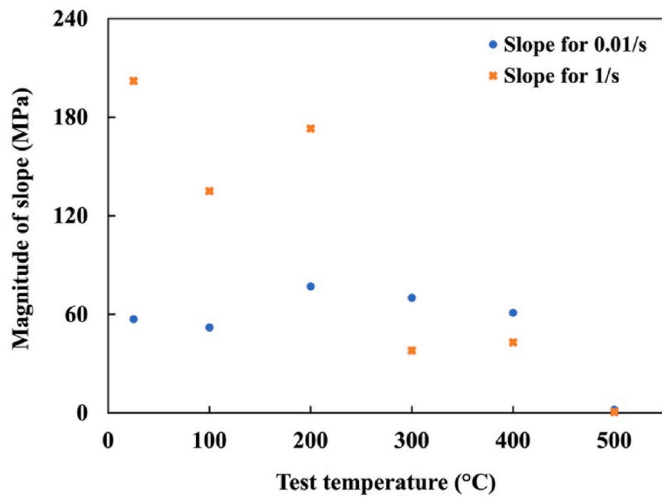


Fig. 3. Slope of the flow stress curves at true strain of 0.4.

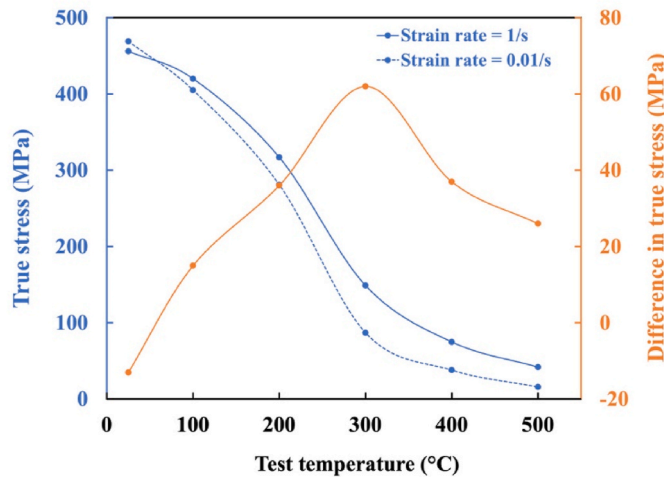


Fig. 4. Variation of flow stress as a function of test temperature at a true strain of 0.4.

obtained by considering only the grains that satisfy the pre-defined conditions.

3. Results

3.1. Flow stress behavior

Fig. 2 shows the true stress-strain curves obtained from the Gleeble tests. The following characteristic feature could be observed from this figure:

- (i) Flow stress level increases with strain rate and decreases with deformation temperature. However, an exception can be noticed in case of RT deformation where the flow stress is higher for 0.01 s⁻¹ than at 1 s⁻¹.

The degree of softening in case of the two strain rates at different deformation temperatures can be comparatively studied from the negative slopes of the flow stress curves after the peak stress level. Simply put, steeper the slope in this region, greater is the extent of softening. Therefore, the slopes of the individual flow stress curves (shown in Fig. 2) at a true strain of 0.4 were calculated, and their magnitudes were plotted against the test temperatures as shown in

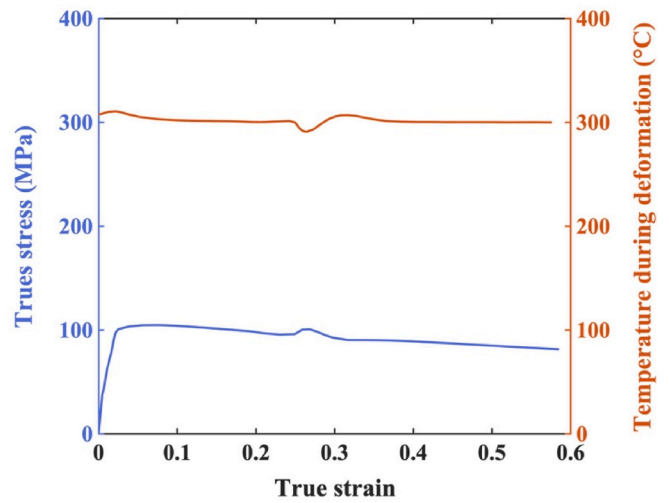


Fig. 5. True stress and measured temperature vs true strain curves for deformation with 0.01 s⁻¹ strain rate at 300 °C.

Fig. 3. It displayed the following characteristic behaviors:

- (ii) In case of deformation up to 200 °C, the material experiences more softening at 1 s⁻¹.
- (iii) Whereas, for deformation at and above 300 °C, the degree of softening is larger for the lower strain rate of 0.01 s⁻¹.

In order to study the manner in which the flow stress varied with temperature, a graph was plotted with flow stress at true strain of 0.4 as a function of test temperature for the two strain rates, which is shown by the primary vertical axis in Fig. 4. The secondary vertical axis in the figure indicates the corresponding difference between the flow stress levels at each test temperature. The figure displayed the following trends which are our next characteristic features:

- (iv) The decrease in the flow stress is enhanced in the temperature region of 200–300 °C for both strain rates.
- (v) The strain rate sensitivity (SRS), which can be roughly estimated by the increase in the flow stress level with increase in strain rate at a constant strain and deformation temperature, is negative at RT, becomes positive and increases with increase in temperature from RT to up to 300 °C and then decreases with further increase in the temperature.

The explanations behind all the above observations are discussed in detail in Section 4.1.

Furthermore, the true stress-strain curves at a strain rate of 0.01 s⁻¹ displayed a distinct hump in the flow stress level for temperatures at and above 200 °C, as indicated by arrow marks in Fig. 2. These humps did not follow any particular trend with respect to temperature or strain. Comparison between these stress-strain curves and the corresponding temperature profile acquired from the thermocouple readings revealed a fluctuation in the temperature level (< ±2%) during the deformation process right over the period when the abrupt jump in the flow stress level occurred. An example of such observation at the deformation temperature of 300 °C is displayed in Fig. 5. Dynamic Systems Inc. (DSI), the manufacturer of the Gleeble machine, confirmed that it is common to obtain this kind of fluctuation in the temperature from the chiller cycling i.e., when the chiller system reaches its control limit. This explains the occurrence of small humps in the flow stress curves for lower strain rate deformation at elevated temperatures. It was inferred that the effect of this temperature fluctuation on the final microstructure after deformation can be neglected since the fluctuation was small and took place during a short time.

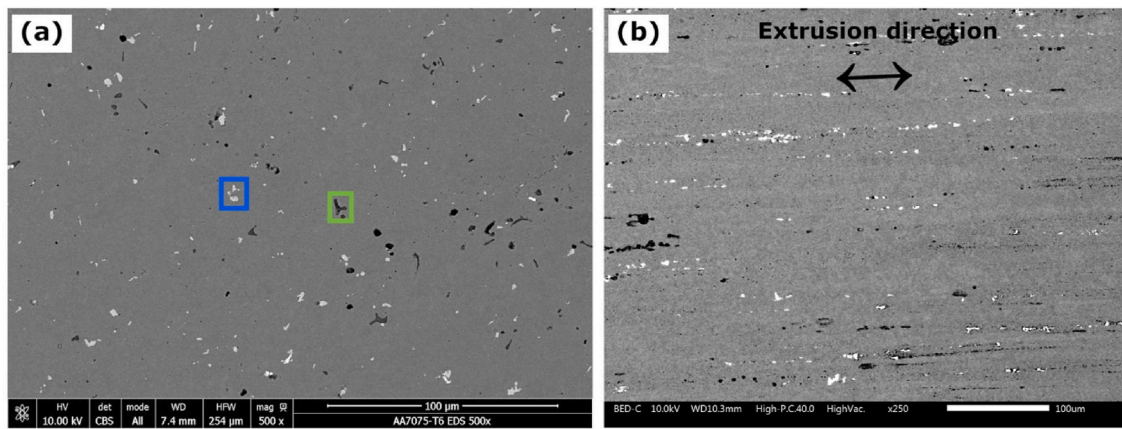


Fig. 6. BSE image of AR AA7075-T651 alloy on (a) TD and (b) LD surfaces.

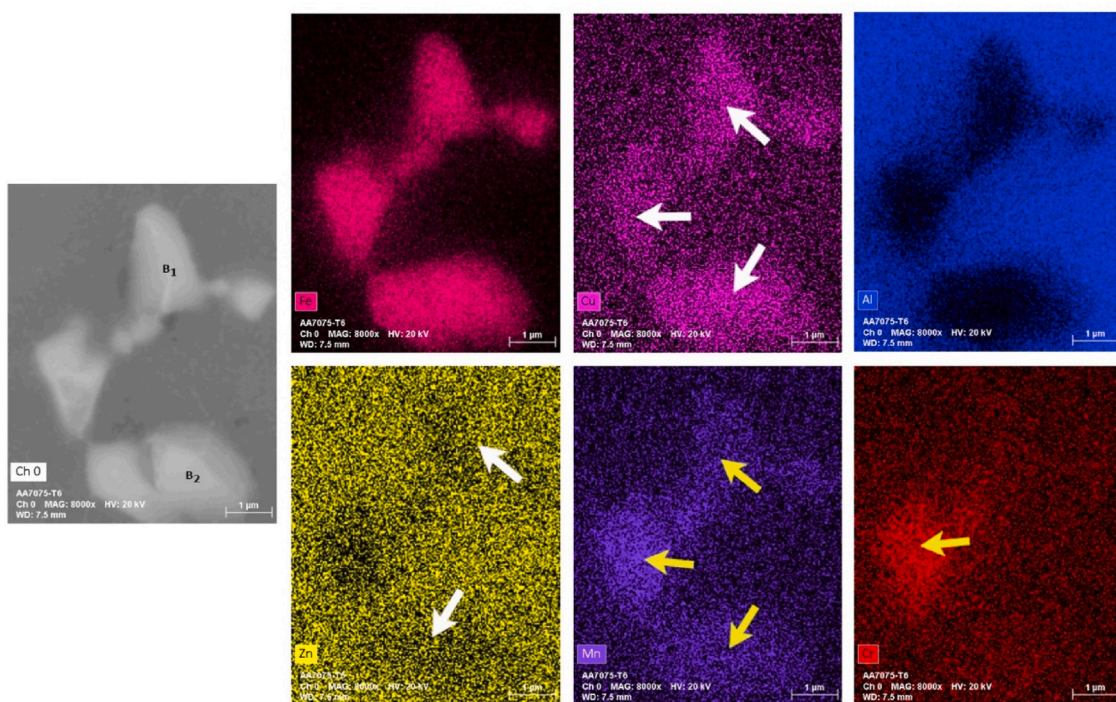


Fig. 7. EDS elemental maps of a bright colored particle present in the matrix. B₁ and B₂ are the locations at which EDS point scans were performed. White arrows indicate the substitution of Al by Cu and Zn. Yellow arrows indicate substitution of Fe by Mn and Cr. (For interpretation of the references to color in this figure legend, the reader is referred to the Web version of this article.)

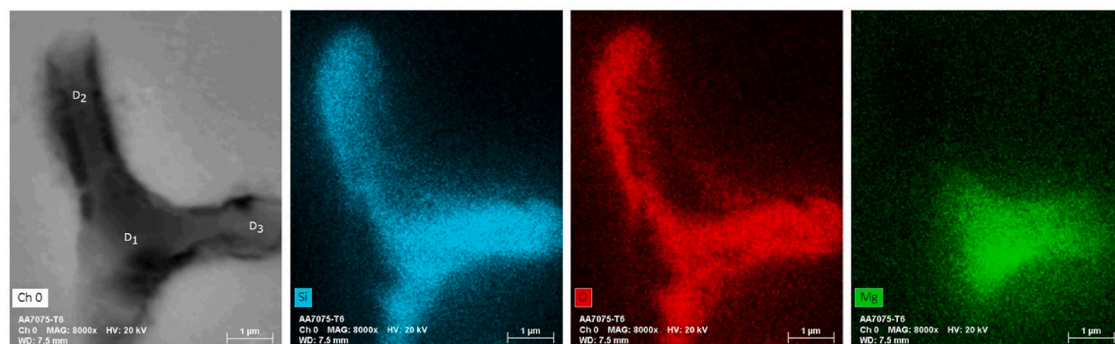


Fig. 8. EDS elemental maps of a dark-colored particle present in the matrix. D₁, D₂ and D₃ are the locations at which EDS point scans were performed.

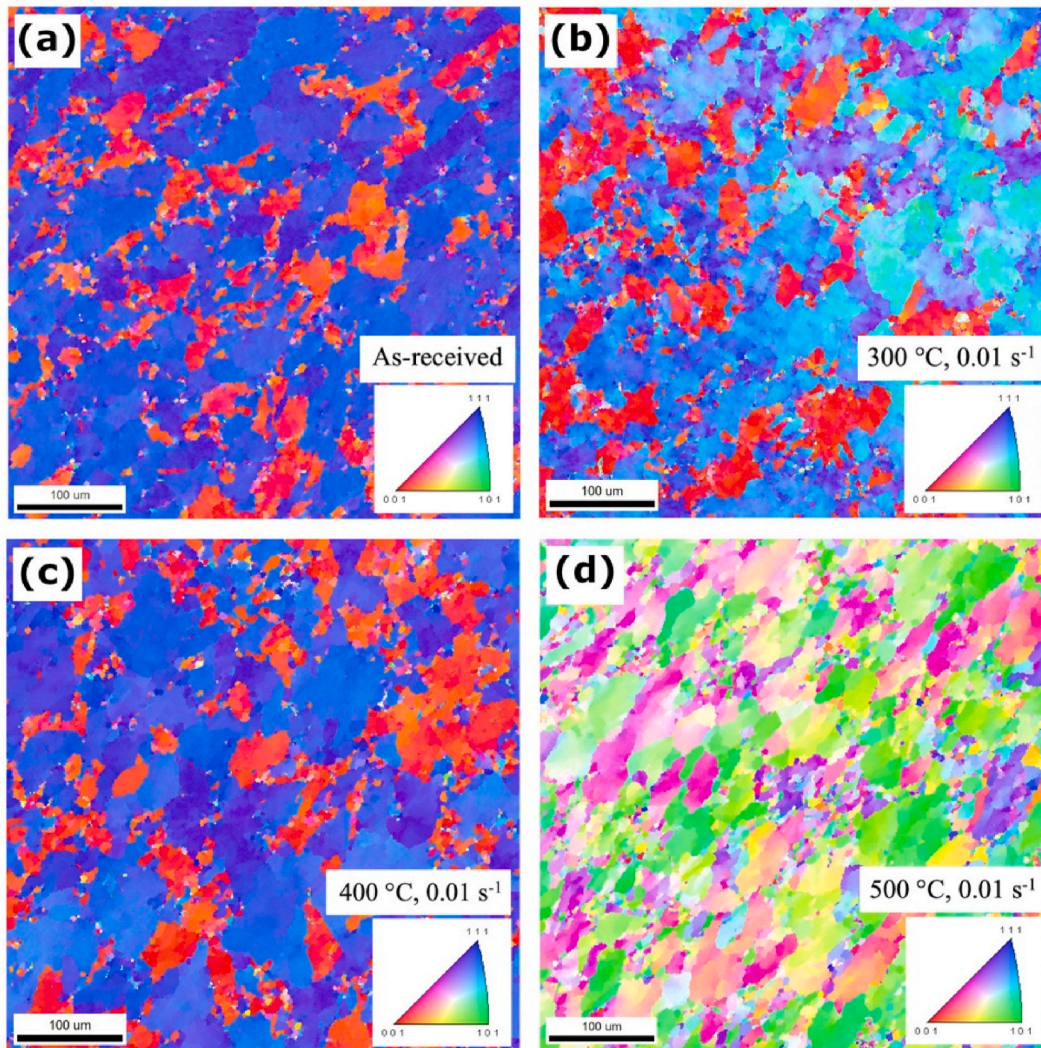


Fig. 9. IPF images obtained at central location on TD surface (a) of AR material, and after deformation with (b) 0.01 s^{-1} at $300 \text{ }^\circ\text{C}$, (c) 0.01 s^{-1} at $400 \text{ }^\circ\text{C}$ and (d) 0.01 s^{-1} at $500 \text{ }^\circ\text{C}$.

3.2. Microstructure characterization

3.2.1. Microstructure of AR material

Fig. 6 shows the BSE image of the matrix of AR AA7075-T651 alloy on two different surfaces. The microstructure on TD surface (Fig. 6 (a)) reveals bright and dark colored irregular shaped intermetallic particles with size ranging between 2 and $10 \mu\text{m}$ distributed throughout the entire matrix. The LD surface (Fig. 6 (b)) displays that these constituent particles are broken up and dispersed along the extrusion direction. Elemental map analyses were performed on number of bright and dark particles in order to determine their type and constitution, which exhibited consistent results. The analyses from representative particles of each type, bright particle inside the blue rectangle and dark particle inside the green rectangle in Fig. 6 (a), are shown in Fig. 7 and Fig. 8, respectively.

From the EDS elemental maps shown in Fig. 7, it can be inferred that the bright intermetallic is rich in Fe as the Fe content is substantially higher in the particle compared to its surrounding matrix. In such Fe-rich intermetallic phases, Cu and Zn can substitute Al while Mn and Cr can substitute Fe [37], which has been indicated by white and yellow arrows respectively in Fig. 7. The average composition of this bright particle obtained from EDS scans at points B₁ and B₂ was found out to be 75.39% Al, 3.59% Zn, 1.68% Mg, 4.58% Cu, 12.37% Fe, 0.71% Mn and

0.34% Cr with Cu:Fe ratio of 0.37 and Al:Fe ratio of 6.09. This could be verified as $(\text{Al,Cu})_6(\text{Fe,Cu})$ phase from its resemblance with the stoichiometric composition reported by Ayer et al. [37]. It is to be noted that Gao et al. [57] have identified the stoichiometric formulae for the same phase as $\text{Al}_{23}\text{CuFe}_4$. The difference in the formula results from the different sources used by the authors in their respective studies.

EDS elemental analysis in Fig. 8 depicts that the dark colored particle is rich in Si and O contents with partial substitution by Mg. The EDS point scans at locations D₁, D₂ and D₃ resulted in an average of 14.12% Si and 19.36% O with Si:O ratio of 0.72. It is identified as SiO_2 phase, as also indicated by other researchers [37,57]. This Si-oxide phase might be argued to be a surface contaminant introduced during the sample preparation. But the studies by Park and Ardell [11] and Ayer et al. [37] reported that the oxide phase is present in the alloy even after ion-milling, suggesting that it is not a contaminant, rather a constituent phase. However, it is not certain if this phase is formed during the alloy melting operation or is already present as an impurity prior to melting.

The intermetallics identified in our AA7075-T651 material are fairly supported by the TEM analyses reported by other researchers [11,37,57]. However, there is a little variation in the composition of the particles that we measured and the ones that are available in the literature. This is due to partial substitution or partitioning of alloying elements within the intermetallics [37,57], as indicated by arrow marks in Fig. 7

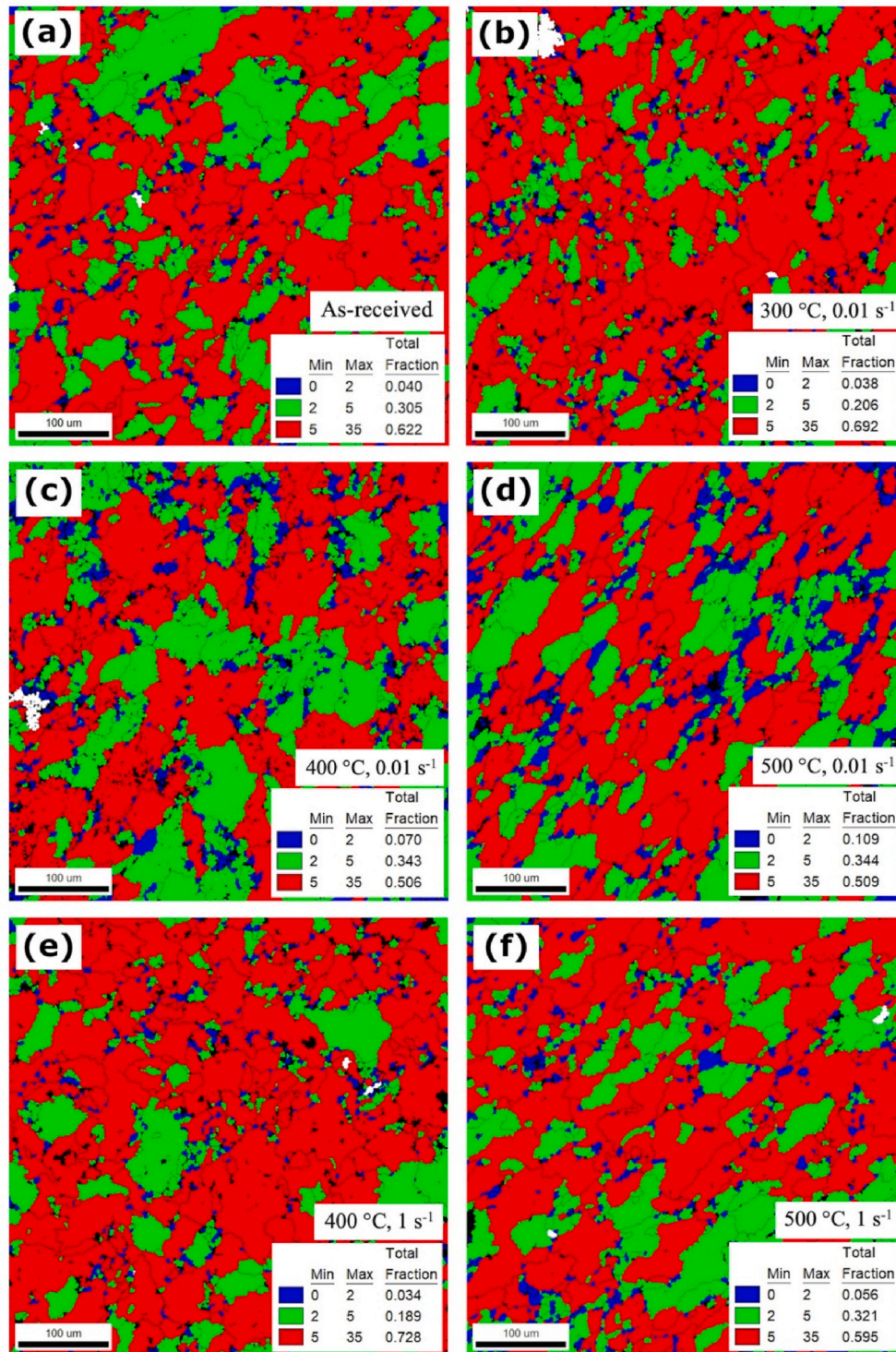


Fig. 10. GOS maps obtained at central location on TD surface (a) of AR material, and after deformation with (b) 0.01 s⁻¹ at 300 °C, (c) 0.01 s⁻¹ at 400 °C, (d) 0.01 s⁻¹ at 500 °C, (e) 1 s⁻¹ at 400 °C and (f) 1 s⁻¹ at 500 °C.

for instance. Furthermore, as already mentioned in Section 2.1, the chemical composition obtained from EDS analysis is only a semi-quantitative presentation without more standardization. Additionally, the results from EDS point scans on intermetallics can also exhibit a contribution from the Al matrix due to the fact that the interaction volume of the electron beam for EDS is larger than the size of the intermetallics.

Some researchers have reported many other intermetallics such as

Al₇Cu₂Fe [4,5,37,58,59], Al₃Fe [59], FeAl₃Si₂ [59], Al₁₂Fe₃Si [37], a modified Al₆Fe [37] and Mg₂Si [4,5,37], but, in the as-cast and solution heat treated states of AA7075, which we did not observe in our peak-aged AA7075. Although Al₇Cu₂Fe and Mg₂Si particles have also been reported in the peak-aged state before [38,60], the literature lacks validation by TEM analysis.

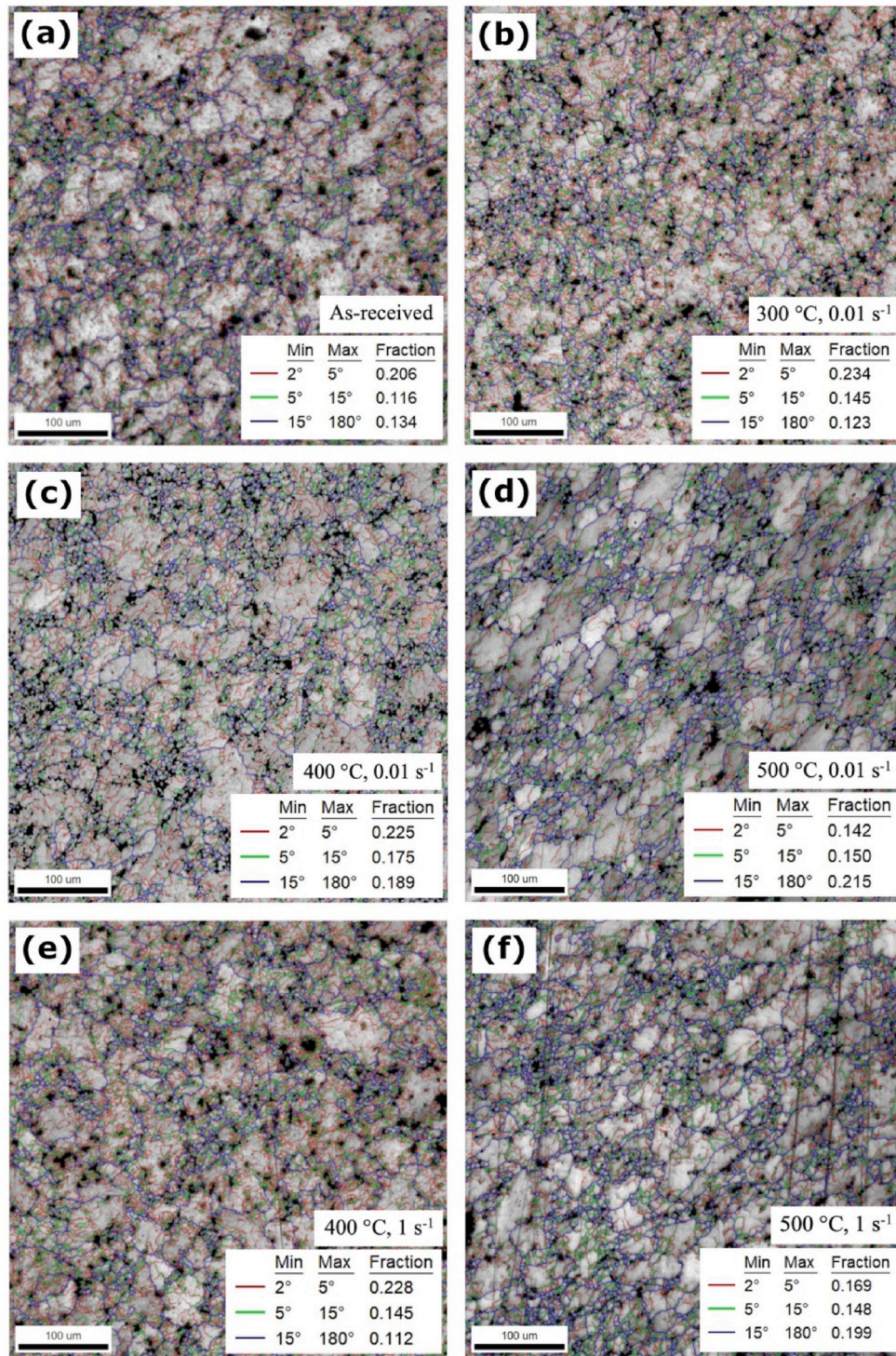


Fig. 11. Grain boundary rotation maps obtained at central location on TD surface (a) of AR material, and after deformation with (b) 0.01 s^{-1} at $300 \text{ }^\circ\text{C}$, (c) 0.01 s^{-1} at $400 \text{ }^\circ\text{C}$, (d) 0.01 s^{-1} at $500 \text{ }^\circ\text{C}$, (e) 1 s^{-1} at $400 \text{ }^\circ\text{C}$ and (f) 1 s^{-1} at $500 \text{ }^\circ\text{C}$.

3.2.2. Microstructure evolution on TD surface

Fig. 9 comprises the IPF images of AA7075-T651 in its AR state and after deformation with 0.01 s^{-1} strain rate at 300, 400 and $500 \text{ }^\circ\text{C}$. These images correspond to the EBSD scans captured at the central location on the TD surface. All the grains in the AR material are seen to be oriented closely along (100) and (111) directions (Fig. 9 (a)). When the material was deformed with 0.01 s^{-1} at $500 \text{ }^\circ\text{C}$, orientation of the grains changed conspicuously, as can be seen from Fig. 9 (d).

Fig. 10 displays the corresponding GOS maps of the IPF images

shown in Fig. 9 along with the ones obtained from the material deformed with 1 s^{-1} strain rate at 400 and $500 \text{ }^\circ\text{C}$. In these maps, the blue colored grains with orientation spread between 0 and 2 represent recrystallized grains. The green colored grains with orientation spread between 2 and 5 and the red colored grains with orientation spread between 5 and 35 represent the deformed and heavily deformed grains, respectively. The grains which have GOS values greater than 35 were not included in the analysis and appear “white” in the maps. The black regions represent the grains that did not fit into the definition of a grain as mentioned in

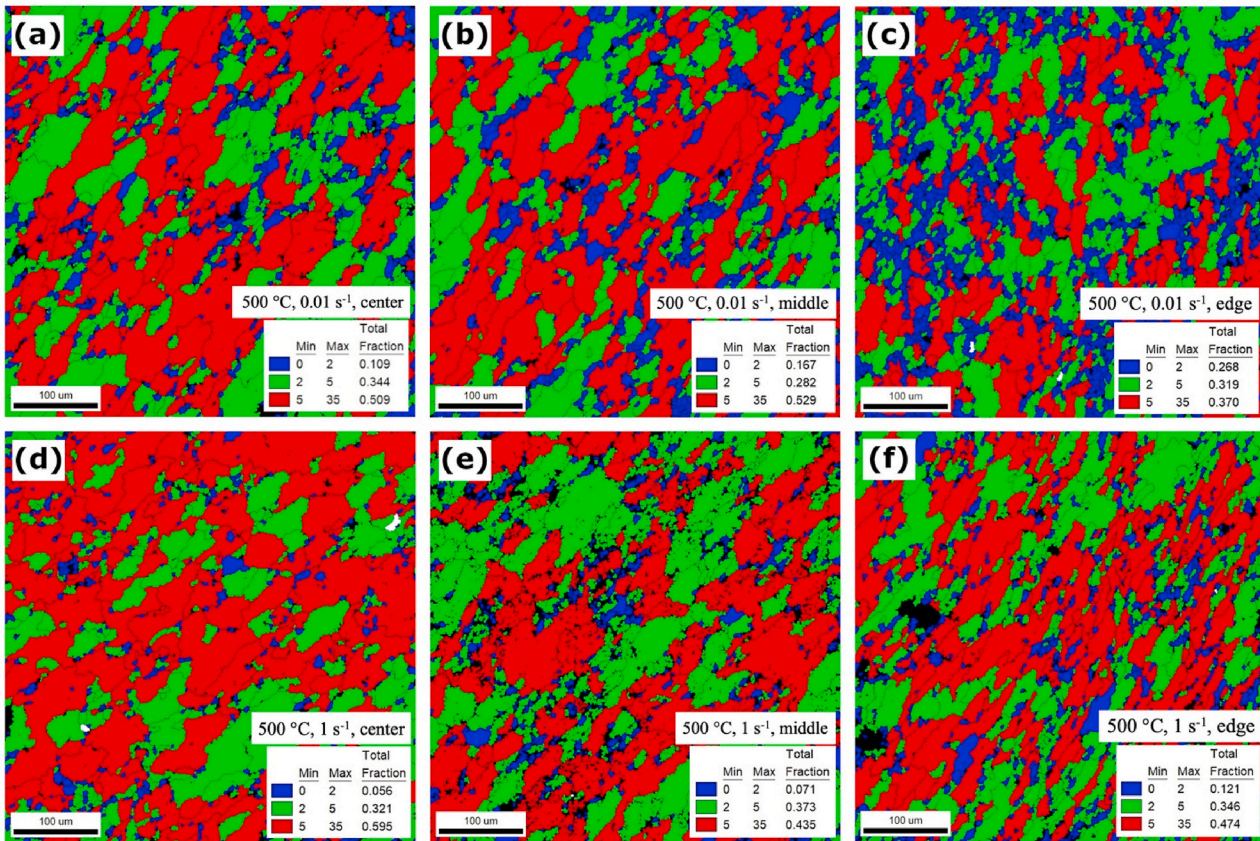


Fig. 12. GOS maps obtained from the TD surface of the material deformed at 500 °C with strain rates of 0.01 s⁻¹ (top row) and 1 s⁻¹ (bottom row). Images taken on the deformed specimens at locations: (a), (d) center, (b), (e) middle, and (c), (f) edge.

Section 2.3. The AR microstructure in Fig. 10 (a) manifests large fraction of deformed and heavily deformed grains and a very small fraction of recrystallized grains developed in the material during the extrusion process. When the material was deformed at 300 °C with 0.01 s⁻¹ (Fig. 10 (b)), no new recrystallized grains were formed. On the other hand, originally deformed grains in the AR state became heavily deformed after the process. As the deformation temperature was increased to 400 and 500 °C for the same strain rate, as shown in Fig. 10 (c) and (d) respectively, new recrystallized grains were formed. When the material was deformed at 400 °C with 1 s⁻¹ (Fig. 10 (e)), fraction of the deformed grains in the AR state turned into heavily deformed grains with no new recrystallized grain formation. However, as the temperature was increased to 500 °C (Fig. 10 (f)), a few new recrystallized grains were formed at the expense of the originally heavily deformed grains. Furthermore, comparison between Fig. 10 (c) and (d) respectively with Fig. 10 (e) and (f) indicates that at a constant temperature, deformation with lower strain rate produced a higher number of recrystallized grains.

Fig. 11 presents the grain boundary rotation maps corresponding to Fig. 10 in order to support the microstructural behavior inferred from the GOS maps. In these maps, the red and green colored lines with boundary rotations between 2° and 15° represent the low angle grain boundaries (LAGB). The LAGB are indicative of sub-grain boundaries formed by arrays of geometrically necessary dislocations (GND) [61]. The blue lines with boundary rotations greater than 15° represent the high angle grain boundaries (HAGB). The black regions are the pores observed on the sample surface along with the grains that did not fit into the definition of a grain as mentioned in Section 2.3. The AR microstructure in Fig. 11 (a) contains both LAGB and HAGB which are developed during extrusion process. When the material was deformed at 300 °C with 0.01 s⁻¹ strain rate (Fig. 11 (b)), fraction of LAGB increased and that of HAGB decreased indicating formation of new LAGB. As the

deformation temperature was increased to 400 °C (Fig. 11 (c)), the fraction of both LAGB and HAGB increased as compared to that in the AR microstructure. Deformation at 500 °C with 0.01 s⁻¹ (Fig. 11 (d)) resulted in decrease in LAGB and a simultaneous increase in the HAGB. When the material was deformed with 1 s⁻¹ at 400 °C (Fig. 11 (e)), new LAGB were formed. Whereas deformation with 1 s⁻¹ at 500 °C (Fig. 11 (f)) displayed an increase in the fraction of HAGB with more or less same fraction of LAGB as compared with the AR state. Furthermore, comparison between Fig. 11 (c) and (d) respectively with Fig. 11 (e) and (f) reveals that at a constant elevated temperature, deformation with lower strain rate produces more HAGB. Increase in the HAGB indicates the formation of new recrystallized grains, thus, their trend with respect to temperatures and strain rates observed from the grain boundary rotation maps in Fig. 11 strongly corroborates with that predicted from the GOS maps in Fig. 10.

The variation in microstructure at different locations was studied by capturing EBSD images at different sites on the same sample surface. The GOS maps obtained from the EBSD scans on the samples deformed at 500 °C with 0.01 and 1 s⁻¹ strain rates are displayed in the top and bottom rows of Fig. 12, respectively. The images on the left, middle and right side of the figure represents the center, middle and edge of the surface, respectively. It can be observed that, in case of both strain rates, the recrystallized grains' fraction increases as we move from the center of the sample towards the edge. Although the RX is not completed, the recrystallized grains start to appear homogeneously towards the edge, conspicuously in case of the material deformed with 0.01 s⁻¹ (Fig. 12 (c)). The fraction of recrystallized grains at a particular location is found to be higher in case of lower strain rate.

3.2.3. Microstructure evolution on LD surface

From the microstructure characterization on the TD surface of the

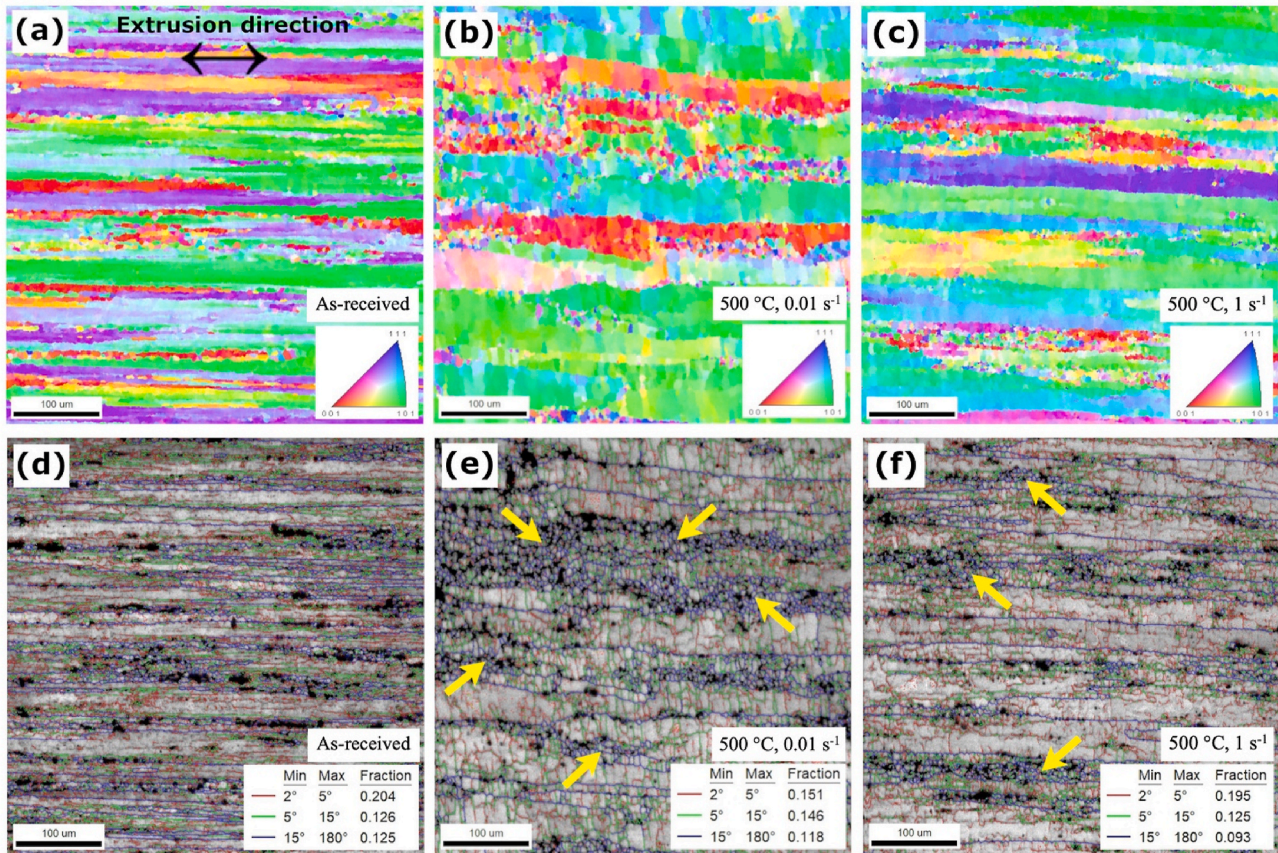


Fig. 13. IPF images (top row) and their corresponding grain boundary maps (bottom row) obtained at central location on LD surface (a), (d) of AR material, and after deformation with (b), (e) 0.01 s^{-1} at $500 \text{ }^\circ\text{C}$ and (c), (f) 1 s^{-1} at $500 \text{ }^\circ\text{C}$. Yellow arrows indicate the formation of new refined grains within the initial columnar grains. (For interpretation of the references to color in this figure legend, the reader is referred to the Web version of this article.)

deformed material, it was observed that the extent of RX seems to be comparatively higher at $500 \text{ }^\circ\text{C}$. Therefore, the microstructures on the LD surface of the material in its AR state and after deformation at $500 \text{ }^\circ\text{C}$ were analyzed, which are shown in Fig. 13. The IPF images (top row in Fig. 13) and their corresponding grain boundary rotation maps (bottom row in Fig. 13) were taken at the central location on LD surface. The AR material has a columnar grain structure elongated along the extrusion axis with grains oriented in different directions as shown in Fig. 13 (a). Similar to the TD surface, the LAGB and HAGB in Fig. 13 (d) are introduced in the material during the extrusion process. When the material is deformed at $500 \text{ }^\circ\text{C}$, the grains are still extended along the extrusion direction (Fig. 13 (b) and (c)), however, unlike the TD surface, there is no conspicuous transformation of the grain orientation from the initial microstructure. Furthermore, refined grains are developed within the initial elongated grains as indicated by yellow arrows in Fig. 13 (e) and (f). On comparing these two figures, it is found that deformation with lower strain rate generated higher fraction of HAGB indicating formation of more recrystallized grains.

Similar to the TD surface, the variation in microstructure at different sites on LD surface was studied from the GOS maps of the samples deformed at $500 \text{ }^\circ\text{C}$ with 0.01 and 1 s^{-1} strain rates which are displayed in the top and bottom rows of Fig. 14, respectively. The images on the left and right side of the figure represents the center and edge of the surface, respectively. The grain structure is elongated along the extrusion direction similar to as shown in Fig. 13. At a constant strain rate, the grains at the central location can be observed to be thicker than those at the edge. Furthermore, the center of the specimen is more heavily deformed than the edge in both the cases. On comparing Fig. 14 (a) and (b) respectively with Fig. 14 (c) and (d), the fraction of recrystallized grains at a particular location is found to be higher in case of lower strain

rate. However, unlike in case of TD surface, here the recrystallized grain fraction does not significantly increase towards the edge of the specimen.

4. Discussion

4.1. Flow stress behavior

Conventionally, the flow stress increases with strain rate and decreases with temperature. However, as mentioned in characteristic feature (i) in Section 3.1, our experimental results depicted a lower flow stress for higher strain rate in case of deformation at RT. In order to investigate the reason behind such behavior, the temperature histories obtained from the thermocouple readings were analyzed, which revealed a continuous increase in the temperature of the material during deformation with 1 s^{-1} for all test temperatures. Fig. 15 shows such rise in temperature in case of compression with 1 s^{-1} at RT and $300 \text{ }^\circ\text{C}$. The temperature attained a maximum of 68 and $314 \text{ }^\circ\text{C}$, respectively, for these two test temperatures. On the other hand, no such rise in temperature is observed for deformation with 0.01 s^{-1} . The appearance of small temperature fluctuation in the curve corresponding to compression with 0.01 s^{-1} at $300 \text{ }^\circ\text{C}$ in Fig. 15 has already been discussed in Section 3.1.

It is well-known that most of the plastic deformation gets converted in to heat during the process. When the material is deformed with higher strain rate, less time is available for dissipation of the heat before the deformation process is completed. The temperature of the material rises due to this “adiabatic heating”, as shown in Fig. 15, and the material experiences thermal softening, which is the reason behind the exceptional behavior mentioned for issue (i) above. Similar adiabatic heating

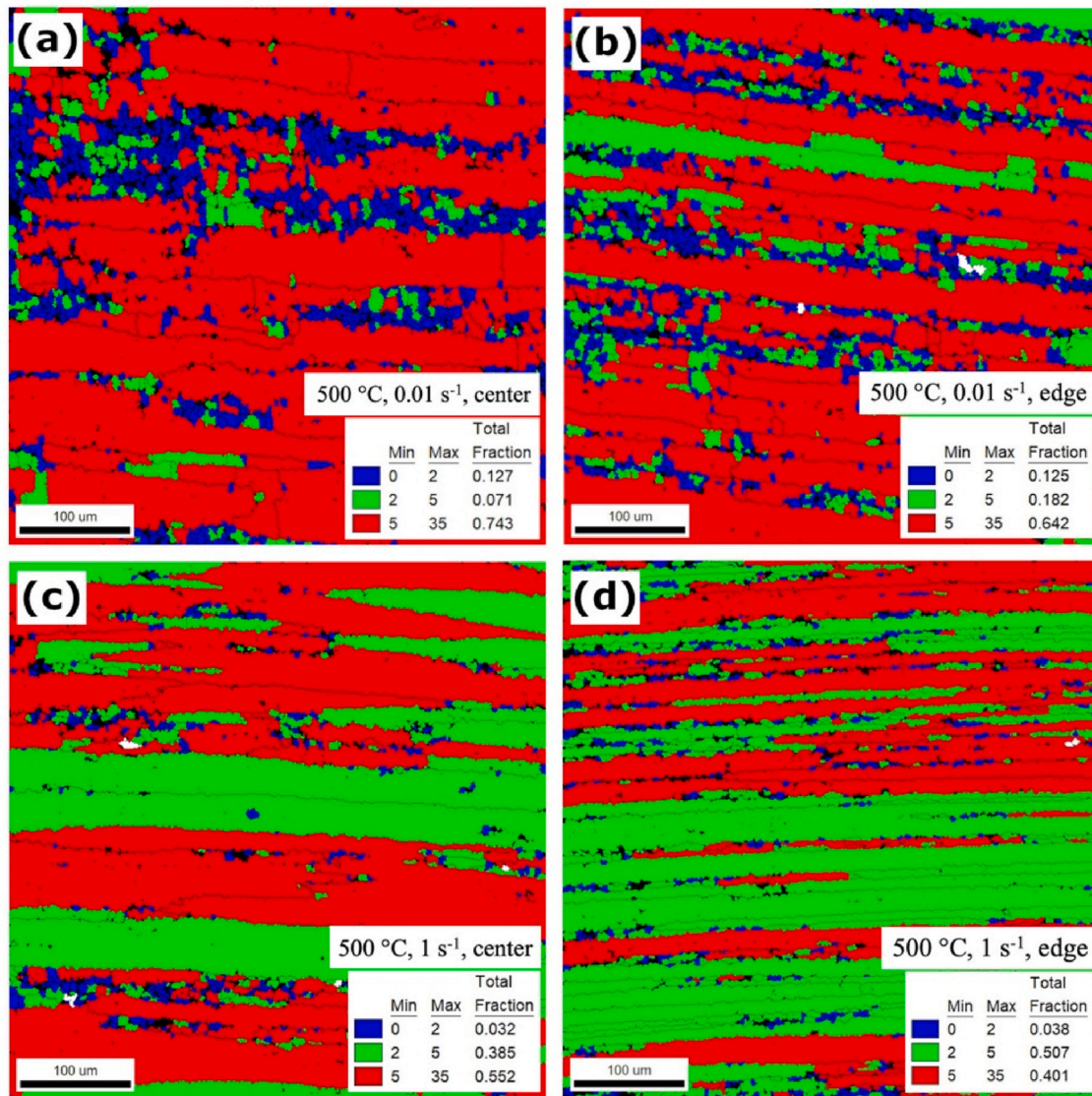


Fig. 14. GOS maps obtained from the LD surface of the material deformed at 500 °C with strain rates of 0.01 s⁻¹ (top row) and 1 s⁻¹ (bottom row). Images taken on the deformed specimens at locations: (a), (c) center, and (b), (d) edge.

effect for deformation at RT has also been reported by other researchers [27,44].

A similar rise in the temperature takes place during deformation with 1 s⁻¹ at elevated temperatures as well. However, at higher deformation temperatures, the flow stress level becomes lower, thereby leading to a lower accumulated heat energy from plastic deformation [49]. As a result, the increase in temperature becomes smaller for higher deformation temperatures, as can be compared between the curves for RT and 300 °C in Fig. 15. Thus, the thermal softening effect arising from adiabatic heating is only significant at lower deformation temperatures. This explains our characteristic feature (ii) which stated that at RT, 100 and 200 °C, higher degree of softening is observed for deformation with higher strain rate of 1 s⁻¹.

When peak-aged AA7075 is deformed at or above 300 °C, most of the strengthening particles are dissolved in the matrix [10,33,35] reducing the resistance against moving dislocations. Furthermore, DRV and DRX become more pronounced in this temperature regime [29,30,39,41,43]. Unlike in case of higher strain rate, the material deformed with lower strain rate has enough time to undergo both of the above phenomena. Thus, for deformation at and above 300 °C, the material experiences greater extent of softening at lower strain rate which is our characteristic

observation (iii).

Engdahl et al. [35] reported that the GP zones are dissolved in the Al matrix at around 150 °C in the presence of more stable precipitates. DeJasi and Adler [33] have shown that the dissolution of GP zones is accompanied by formation and growth of η' precipitates under 217 °C. The η' precipitates dissolve in the matrix within a temperature range of 217–271 °C with simultaneous formation and growth of the stable η precipitates. And these η precipitates dissolve in the Al matrix above a temperature of 271 °C. The progressive coarsening, transformation and dissolution of all these strengthening precipitates lead to the softening of the alloy which can account for the enhanced drop in the flow stress at around 200 and 300 °C, as mentioned in the characteristic feature (iv). Additionally, it can also be observed from Fig. 4 that the flow stress follows quite similar pattern with respect to the deformation temperature for both the strain rates, which indicates that the temperature sensitivity of our material is independent of the strain rate. Similar behavior of flow stress has also been reported for deformation at strain rates different than ours [24,47].

The negative SRS for deformation at RT is attributed to the adiabatic heating effect which has been discussed above. Previously researchers have reported that the SRS of AA7075 becomes more pronounced when

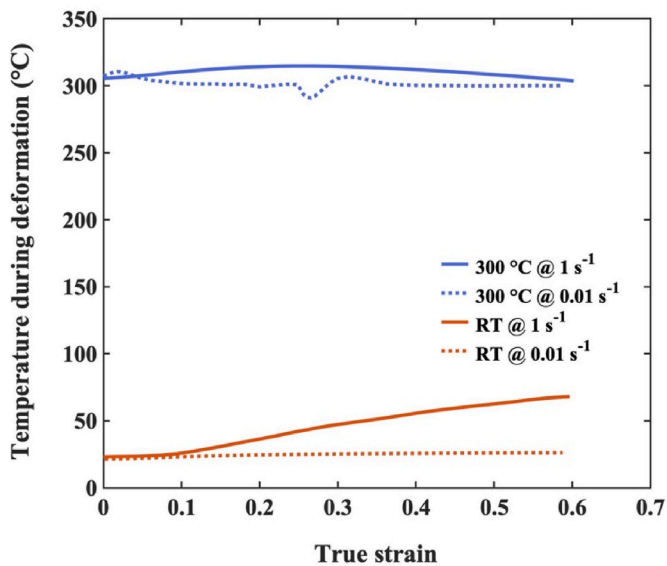


Fig. 15. Temperature profile from thermocouple readings during deformation at RT and 300 °C.

deformation temperature is increased up to 300 °C [21,29]. Whereas, as already mentioned, softening due to dissolution of precipitates, DRV and DRX starts to progressively dominate over the effect of hardening beyond this temperature. Therefore, the SRS is negative at RT, increases up to 300 °C and decreases thereafter, as pointed out in attribute (v). Similar trend of SRS can be observed in the study by Zhou et al. [31]. In contrast, Taheri et al. [47] has reported a continuous increase in SRS with increase in deformation temperature from 100 to 500 °C.

4.2. Effect of temperature and strain rate on DRX

The fraction of the recrystallized grains from the GOS maps shown in Fig. 10 and the fractions of LAGB and HAGB from the grain boundary rotation maps shown in Fig. 11 have been consolidated in Fig. 16. Extrusion process induces dislocations in the material that rearrange themselves to form subgrains with LAGB [36], whose fraction is shown for the AR state in Fig. 16. The corresponding fraction of HAGB depicts the initial grains including the recrystallized ones produced during the extrusion process. When the material is deformed with 0.01 s⁻¹ at 300 °C and with 1 s⁻¹ at 400 °C, the fraction of LAGB is increased which indicates formation of sub-grains within the original grains via rearrangements of GNDs, implicating DRV mechanism. The corresponding HAGB fractions do not vary much from that of the AR state, suggesting

the absence of DRX for the above two deformation conditions, which is also supported by the more or less same fraction of recrystallized grains in the respective states. The mobility of the grain boundaries is not high enough at 300 °C to activate DRX. Moreover, the presence of undissolved strengthening precipitates and dispersoids also restricts the grain boundary mobility, thereby preventing DRX from taking place at these deformation conditions. Whereas, when the deformation is carried out with 0.01 s⁻¹ at 400 °C, it can be deduced that DRV is still going on via formation of subgrain clusters, thus, increasing the fraction of LAGB. In addition, at this reduced strain rate of 0.01 s⁻¹, the material has enough time for the stable strengthening particles to get dissolved. As the deformation temperature is further increased to 500 °C for both 0.01 and 1 s⁻¹ strain rates, the dispersoids, that are usually found in the peak-aged states of AA7075, also get dissolved in the matrix [5,6,36]. The dissolution of these second phase precipitates lead to weakening of the grain boundary pinning effect in the above three deformation conditions. Furthermore, the thermal energy developed at these higher temperatures significantly enhances the diffusion of atoms within the material stimulating the dislocation mobility. The reduction in grain boundary pinning and promotion of dislocation mobility together lead to subgrain rotation, supposedly via grain boundary sliding (GBS) [43] and absorption of dislocations into subgrain boundaries [30,41]. Thus, subgrains having LAGB are continuously transformed into new recrystallized fine grains, shown as an increase in the fraction of HAGB as well as that of recrystallized grains for the material deformed with 0.01 s⁻¹ at 400 and 500 °C, and with 1 s⁻¹ at 500 °C. This progressive transformation of LAGB into HAGB depicts the typical characteristic of CDRX phenomenon [53,62–64].

When a material is manufactured by large deformation in one-direction, in our case extrusion, significant grain elongation takes place along the deformation direction with thinning of grains along the radial direction, which can be observed in Fig. 13 (a). When the material is then deformed, DRV acts as the dominant softening mechanism at lower deformation temperatures since the mobility of HAGB is too low to migrate to form serrations [53]. As the deformation temperature increases, it significantly promotes the diffusion of atoms. Also, the second phase precipitates start to dissolve in the matrix and the grain boundary pinning effect is reduced. As a result, the initial elongated grain boundaries become more and more serrated as the deformation progresses. When the strain produced in the material is sufficient, the serrated boundaries are pinched off to form new refined grains, as can be observed in Fig. 13 (e) and (f), depicting a typical GDRX phenomenon [53,62,64].

The continuous transformation of LAGB into HAGB in case of CDRX and the serration and migration of original grain boundaries in case of GDRX need sufficient time to take place [41]. When the material is deformed with lower strain rate, more time is available for the thermally

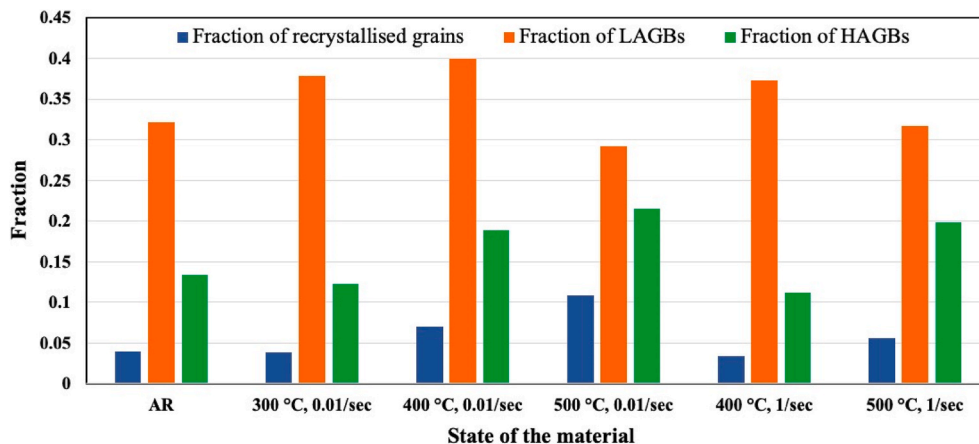


Fig. 16. Fraction of recrystallized grains, LAGB and HAGB observed on the TD surface of AR and different deformed states of the material.

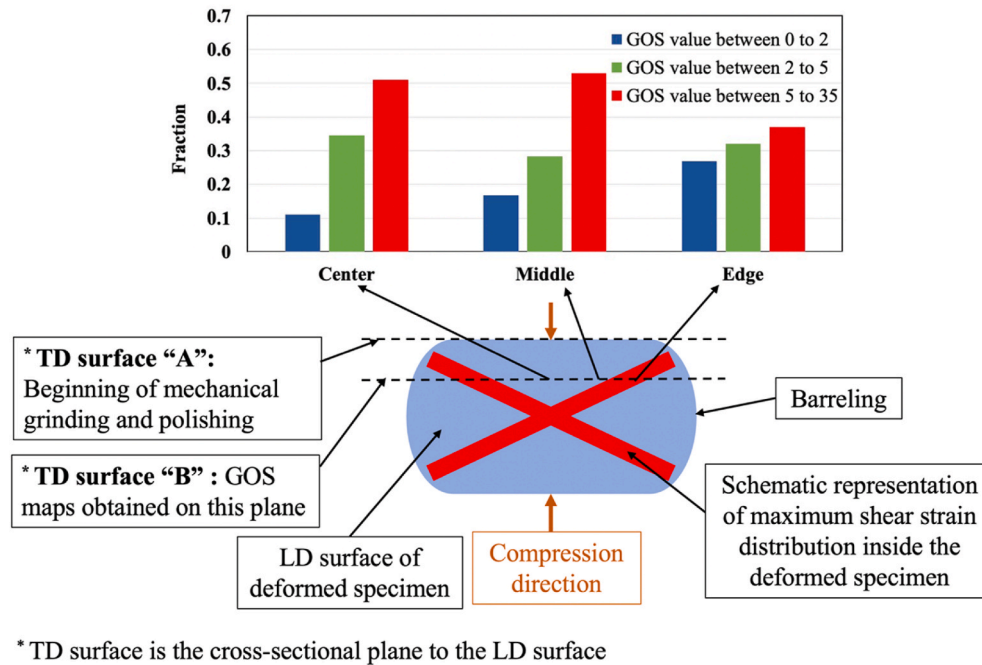


Fig. 17. Schematic representation of maximum shear strain distribution inside the deformed specimen and the GOS maps obtained from different locations on the TD surface.

activated mechanisms to take place and drive the DRX mechanisms to greater extent. Therefore, at a given deformation temperature, lower strain rate produces higher degree of DRX, as depicted in all the GOS and grain boundary rotation maps reported in this study. Consequently, the degree of softening is higher for 0.01 s^{-1} when compared to 1 s^{-1} at deformation temperatures of $300 \text{ }^\circ\text{C}$ and above, which is reflected in the flow stress behavior.

4.3. Effect of location on microstructure evolution

The greater number of deformed and heavily deformed grains displayed by the GOS maps in Fig. 10, Fig. 12 and Fig. 14 indicates that DRX was not completed during the deformation. Furthermore, the inhomogeneous distribution of the refined grains in these figures suggests that the RX took place in local areas depending on local plastic deformation. Different locations within the material sample experience different local strain levels due to the “barreling” caused by the friction at the contact surfaces between the anvils of the machine and the sample. More generally, the material points can experience different local stress and strain states depending upon their positions on the planes perpendicular to the compression direction, which is demonstrated below.

The increasing degree of RX towards the edge on the TD surface, as shown in Fig. 12, can be explained with the help of Fig. 17. It consists of a schematic representation of maximum shear strain distribution in the material during the deformation and a histogram distribution of GOS fractions from three different approximate locations on the TD surface after deformation with 0.01 s^{-1} at $500 \text{ }^\circ\text{C}$ (corresponding to the GOS maps in the top row of Fig. 12). The schematic diagram of inhomogeneous strain distribution on LD surface is a derivative of the simulation of the shear bands formation during the compression tests reported by other researchers [65–68]. When a deformed specimen is selected for EBSD observation on TD surface (cross-sectional plane to the LD surface, as indicated by dashed line in Fig. 17), the metallographic sample preparation is started with mechanical grinding at plane “A” and is finished with electropolishing at round about plane “B”. When the EBSD scans are run at three different locations on the TD surface “B”, the central location supposedly corresponds to a region with comparatively less shear strain. The middle position lies in the proximity of the strain

distribution, thereby experiencing a bit more local deformation compared to the center. Whereas the edge of the specimen is located more or less within the spread and experiences comparatively the largest shear strain. As the location is gradually shifted from the center to the edge position, the histogram displays a corresponding increase in the fraction of the recrystallized grains that are represented by GOS value between 0 and 2. Previously, researchers have shown that the extent of DRX increases with increase in the strain produced in AA7075 during hot deformation [29,41,43], which justifies our observation of increasing fraction of recrystallized grains with increasing shear strain towards the edge of the sample.

The LD surface in Fig. 14 displayed that the elongated grains are thicker at the center of the deformed samples. This microstructure was imparted during the initial “drawing” process, and this distribution of grain morphology was maintained even after the hot deformation.

5. Conclusions

The mechanical and microstructural behavior of AA7075-T651 alloy during deformation with 0.01 and 1 s^{-1} strain rates at different temperatures from RT up to $500 \text{ }^\circ\text{C}$ have been studied and analyzed using Gleeble thermo-mechanical simulator and SEM. The following conclusions have been drawn from the current research work:

- The flow stress increases with strain rate and decreases with temperature as expected. However, the flow stress for deformation at RT is lower at higher strain rate due to adiabatic heating.
- The material experiences greater extent of softening for higher strain rate up to a temperature of $200 \text{ }^\circ\text{C}$. Whereas, at elevated temperatures of $300 \text{ }^\circ\text{C}$ and above, the extent of softening is more in case of lower strain rate.
- The significant changes in the microstructure with respect to the strengthening precipitates result in an enhanced decrease in the flow stress for both strain rates at around $200\text{--}300 \text{ }^\circ\text{C}$.
- SRS is negative at RT, becomes positive and increases with increase in temperature from RT up to $300 \text{ }^\circ\text{C}$ and decreases afterwards.
- Observation with SEM revealed two types of intermetallic particles in the AR material: $(\text{Al,Cu})_6(\text{Fe,Cu})$ and SiO_2 .

- DRV is the major softening mechanism for deformation with 0.01 s^{-1} at $300 \text{ }^\circ\text{C}$ and 1 s^{-1} at $400 \text{ }^\circ\text{C}$. Both DRV and DRX are found to be occurring simultaneously for deformation with 0.01 s^{-1} at $400 \text{ }^\circ\text{C}$. Deformation at $500 \text{ }^\circ\text{C}$ exhibits DRX for both the strain rates.
- DRX observed in this research is incomplete and takes place in local areas as a combination of CDRX and GDRX mechanisms. Furthermore, the degree of DRX is found to increase in case of deformation with higher temperature and lower strain rate.
- Depending on the location on the specimen, different material points experience different degree of local plastic strain and thereby corresponding degree of DRX.

The current study covers the flow stress behavior with respect to strain rate and temperature sensitivity at 0.01 and 1 s^{-1} strain rates over the entire range of temperature between RT and $500 \text{ }^\circ\text{C}$. In addition, the EBSD analysis gives a better understanding about the effects of temperature and strain rate on the microstructure evolution after the deformation. The results obtained from both mechanical and microstructural characterizations will be used to develop a physics-based material model for AA7075-T651 that can predict the final state of the material at the end of the manufacturing chain.

Data availability

The raw and processed data required to reproduce these findings cannot be shared at this time as the data also forms part of an ongoing study.

CRedit authorship contribution statement

Biswajit Dalai: Methodology, Investigation, Formal analysis, Writing – original draft, Visualization. **Marie Anna Moretti:** Investigation, Formal analysis, Writing – review & editing. **Paul Åkerström:** Methodology, Investigation, Writing – review & editing, Supervision. **Corinne Arvieu:** Writing – review & editing, Supervision. **Dimitri Jacquin:** Conceptualization, Writing – review & editing, Supervision. **Lars-Erik Lindgren:** Conceptualization, Writing – review & editing, Supervision.

Declaration of competing interest

The authors declare that they have no known competing financial interests or personal relationships that could have appeared to influence the work reported in this paper.

Acknowledgements

This research work is a part of the ENABLE project funded by the European Union's Marie Skłodowska-Curie Actions (MSCA) Innovative Training Networks (ITN) H2020-MSCA-ITN-2017 under the grant agreement No 764979. The authors would like to thank Alumeco for providing the material used for experimental studies. They are also grateful to the Division of Materials Science, Luleå University of Technology, Sweden and the Centre des Matériaux, MINES ParisTech, France for allowing to use their laboratories and equipment for carrying out the experiments. Finally, the authors would like to thank Dr. Valdimir Esin, Centre des Matériaux, MINES ParisTech, France for his helpful comments on the EBSD analysis.

References

- [1] Heat treating of aluminum alloys, ASM Handb., 1991, pp. 841–879, <https://doi.org/10.1361/asmhba000>.
- [2] R.F. Muraca, J.S. Whittick (Eds.), *Materials Data Handbook: Aluminum Alloy 7075*, second ed., Western Applied Research & Development, San Carlos, California, 1972.
- [3] J.G. Kaufman, Understanding the aluminum temper designation system, in: *Introduct. To Alum. Alloy. Tempers*, ASM International, 2000, pp. 39–76. https://aluminium-guide.com/wp-content/uploads/2019/04/j._gilbert_kaufman_introduction_to_a_luminum_allobookfi.org_.pdf.
- [4] N. Mahathaninwong, T. Plookphol, J. Wannasin, S. Wisutmethangoon, T6 heat treatment of rheocasting 7075 Al alloy, *Mater. Sci. Eng., A* 532 (2012) 91–99, <https://doi.org/10.1016/j.msea.2011.10.068>.
- [5] X. Zou, H. Yan, X. Chen, Evolution of second phases and mechanical properties of 7075 Al alloy processed by solution heat treatment, *Trans. Nonferrous Met. Soc. China* (English Ed. 27 (2017) 2146–2155, [https://doi.org/10.1016/S1003-6326\(17\)60240-1](https://doi.org/10.1016/S1003-6326(17)60240-1).
- [6] Q. Liu, S. Chen, R. Gu, W. Wang, X. Wei, Effect of heat treatment conditions on mechanical properties and precipitates in sheet metal hot stamping of 7075 aluminum alloy, *J. Mater. Eng. Perform.* 27 (2018) 4423–4436, <https://doi.org/10.1007/s11665-018-3588-z>.
- [7] H.H. Kim, C.G. Kang, Evaluation of precipitation hardening characteristics of rheology-forged Al 7075 aluminum alloy using nano- or microindentation and atomic force microscopy, *Metall. Mater. Trans., A* 41 (2010) 696–705, <https://doi.org/10.1007/s11661-009-0074-0>.
- [8] J.D. Embury, R.B. Nicholson, The nucleation of precipitates: the system Al-Zn-Mg, *Acta Metall.* 13 (1965) 403–417, [https://doi.org/10.1016/0001-6160\(65\)90067-2](https://doi.org/10.1016/0001-6160(65)90067-2).
- [9] H. Löffler, I. Kovacs, J. Lendvai, Decomposition processes in Al-Zn-Mg alloys, *J. Mater. Sci.* 18 (1983) 2215–2240. <https://link.springer.com/content/pdf/10.1007%2FBF00541825.pdf>.
- [10] L.F. Mondolfo, N.A. Gjostein, D.W. Levinson, Structural changes during the aging in an Al-Mg-Zn alloy, *JOM* 8 (1956) 1378–1385, <https://doi.org/10.1007/BF03377889>.
- [11] J.K. Park, A.J. Ardell, Microstructures of the commercial 7075 Al alloy in the T651 and T7 tempers, *Metall. Trans., A* 14 (1983) 1957–1965, <https://doi.org/10.1007/BF02662363>.
- [12] J.K. Park, A.J. Ardell, Precipitation at grain boundaries in the commercial alloy Al 7075, *Acta Metall.* 34 (1986) 2399–2409, [https://doi.org/10.1016/0001-6160\(86\)90143-4](https://doi.org/10.1016/0001-6160(86)90143-4).
- [13] J.K. Park, A.J. Ardell, Precipitate microstructure of peak-aged 7075 Al, *Scripta Metall.* 22 (1988) 1115–1119, [https://doi.org/10.1016/S0036-9748\(88\)80114-5](https://doi.org/10.1016/S0036-9748(88)80114-5).
- [14] T. Dursun, C. Soutis, Recent developments in advanced aircraft aluminum alloys, *Mater. Des.* 56 (2014) 862–871, <https://doi.org/10.1016/j.matdes.2013.12.002>.
- [15] Aerospace Specification Metals Inc., 2018. <https://web.archive.org/web/20181016063536/http://asm.matweb.com/search/SpecificMaterial.asp?bassnum=MA7075T6>. (Accessed 14 April 2021).
- [16] E.A. Starke, J.T. Staley, Application of modern aluminium alloys to aircraft, in: *Fundam. Alum. Metall*, Elsevier, 2011, pp. 747–783, <https://doi.org/10.1533/9780857090256.3.747>.
- [17] M.R. Rokni, A. Zarei-Hanzaki, A.A. Roostaei, A. Abolhasani, Constitutive base analysis of a 7075 aluminum alloy during hot compression testing, *Mater. Des.* 32 (2011) 4955–4960, <https://doi.org/10.1016/j.matdes.2011.05.040>.
- [18] G.Z. Quan, Y.P. Mao, G.S. Li, W.Q. Lv, Y. Wang, J. Zhou, A characterization for the dynamic recrystallization kinetics of as-extruded 7075 aluminum alloy based on true stress-strain curves, *Comput. Mater. Sci.* 55 (2012) 65–72, <https://doi.org/10.1016/j.commatsci.2011.11.031>.
- [19] H.T. Jeong, W.J. Kim, Comparison of hot deformation behavior characteristics between as-cast and extruded Al-Zn-Mg-Cu (7075) aluminum alloys with a similar grain size, *Materials* (Basel) 12 (2019) 1–16, <https://doi.org/10.3390/ma122333807>.
- [20] S.Y. Park, W.J. Kim, Difference in the hot compressive behavior and processing maps between the as-cast and homogenized Al-Zn-Mg-Cu (7075) alloys, *J. Mater. Sci. Technol.* 32 (2016) 660–670, <https://doi.org/10.1016/j.jmst.2016.04.006>.
- [21] Y.C. Lin, L.-T. Li, Y.-X. Fu, Y.-Q. Jiang, Hot compressive deformation behavior of 7075 Al alloy under elevated temperature, *J. Mater. Sci.* 47 (2012) 1306–1318, <https://doi.org/10.1007/s10853-011-5904-y>.
- [22] H. Mirzadeh, Simple physically-based constitutive equations for hot deformation of 2024 and 7075 aluminum alloys, *Trans. Nonferrous Met. Soc. China* (English Ed. 25 (2015) 1614–1618, [https://doi.org/10.1016/S1003-6326\(15\)63765-7](https://doi.org/10.1016/S1003-6326(15)63765-7).
- [23] H. Mirzadeh, Constitutive description of 7075 aluminum alloy during hot deformation by apparent and physically-based approaches, *J. Mater. Eng. Perform.* 24 (2015) 1095–1099, <https://doi.org/10.1007/s11665-015-1389-1>.
- [24] W.-S. Lee, W.-C. Sue, C.-F. Lin, C.-J. Wu, The strain rate and temperature dependence of the dynamic impact properties of 7075 aluminum alloy, *J. Mater. Process. Technol.* 100 (2000) 116–122, [https://doi.org/10.1016/S0924-0136\(99\)00465-3](https://doi.org/10.1016/S0924-0136(99)00465-3).
- [25] G.Z. Quan, K.W. Liu, J. Zhou, B. Chen, Dynamic softening behaviors of 7075 aluminum alloy, *Trans. Nonferrous Met. Soc. China* (English Ed. 19 (2009) 537–541, [https://doi.org/10.1016/S1003-6326\(10\)60104-5](https://doi.org/10.1016/S1003-6326(10)60104-5).
- [26] M. Sasso, A. Forcelllese, M. Simoncini, D. Amodio, E. Mancini, High strain rate behaviour of AA7075 aluminum alloy at different initial temper states, *key eng. Mater.* <https://doi.org/10.4028/www.scientific.net/KEM.651-653.114>, 2015, 651–653, 11–119.
- [27] E. El-Magd, M. Abouridouane, Characterization, modelling and simulation of deformation and fracture behaviour of the light-weight wrought alloys under high strain rate loading, *Int. J. Impact Eng.* 32 (2006) 741–758, <https://doi.org/10.1016/j.ijimpeng.2005.03.008>.
- [28] G. Quan, G. Li, Y. Wang, W. Lv, C. Yu, J. Zhou, A characterization for the flow behavior of as-extruded 7075 aluminum alloy by the improved Arrhenius model with variable parameters, *Mater. Res.* 16 (2012) 19–27, <https://doi.org/10.1590/S1516-14392012005000156>.

- [29] W. Xiao, B. Wang, Y. Wu, X. Yang, Constitutive modeling of flow behavior and microstructure evolution of AA7075 in hot tensile deformation, *Mater. Sci. Eng., A* 712 (2018) 704–713, <https://doi.org/10.1016/j.msea.2017.12.028>.
- [30] Z.C. Sun, H.L. Wu, J. Cao, Z.K. Yin, Modeling of continuous dynamic recrystallization of Al-Zn-Cu-Mg alloy during hot deformation based on the internal-state-variable (ISV) method, *Int. J. Plast.* 106 (2018) 73–87, <https://doi.org/10.1016/j.jiplas.2018.03.002>.
- [31] P. Zhou, Y. Song, L. Hua, J. Lu, J. Zhang, F. Wang, Mechanical behavior and deformation mechanism of 7075 aluminum alloy under solution induced dynamic strain aging, *Mater. Sci. Eng., A* 759 (2019) 498–505, <https://doi.org/10.1016/j.msea.2019.05.071>.
- [32] P. Zhou, Y. Song, L. Hua, J. Lin, J. Lu, Using novel strain aging kinetics models to determine the effect of solution temperature on critical strain of Al-Zn-Mg-Cu alloy, *J. Alloys Compd.* 838 (2020), <https://doi.org/10.1016/j.jallcom.2020.155647>, 155647.
- [33] R. Delasi, P.N. Adler, Calorimetric studies of 7000 series aluminum alloys: I. Matrix precipitate characterization of 7075, *Metall. Trans., A* 8 (1977) 1177–1183, <https://doi.org/10.1007/BF02667403>.
- [34] J.K. Park, A.J. Ardell, Correlation between microstructure and calorimetric behavior of aluminum alloy 7075 and Al-Zn-Mg alloys in various tempers, *Mater. Sci. Eng., A* 114 (1989) 197–203, [https://doi.org/10.1016/0921-5093\(89\)90859-9](https://doi.org/10.1016/0921-5093(89)90859-9).
- [35] T. Engdahl, V. Hansen, P. Warren, K. Stiller, Investigation of fine scale precipitates in Al-Zn-Mg alloys after various heat treatments, *Mater. Sci. Eng., A* 327 (2002) 59–64, [https://doi.org/10.1016/S0921-5093\(01\)01876-7](https://doi.org/10.1016/S0921-5093(01)01876-7).
- [36] P.A. Rometsch, Y. Zhang, S. Knight, Heat treatment of 7xxx series aluminum alloys—some recent developments, *Trans. Nonferrous Metals Soc. China* 24 (2014) 2003–2017, [https://doi.org/10.1016/S1003-6326\(14\)63306-9](https://doi.org/10.1016/S1003-6326(14)63306-9).
- [37] R. Ayer, J.Y. Koo, J.W. Steeds, B.K. Park, Microanalytical study of the heterogeneous phases in commercial Al-Zn-Mg-Cu alloys, *Metall. Trans., A* 16 (1985) 1925–1936, <https://doi.org/10.1007/BF02662393>.
- [38] F. Andreatta, H. Terry, J.H.W. de Wit, Effect of solution heat treatment on galvanic coupling between intermetallics and matrix in AA7075-T6, *Corrosion Sci.* 45 (2003) 1733–1746, [https://doi.org/10.1016/S0010-938X\(03\)00004-0](https://doi.org/10.1016/S0010-938X(03)00004-0).
- [39] M.R. Rokni, A. Zarei-Hanzaki, A.A. Roostaei, H.R. Abedi, An investigation into the hot deformation characteristics of 7075 aluminum alloy, *Mater. Des.* 32 (2011) 2339–2344, <https://doi.org/10.1016/j.matdes.2010.12.047>.
- [40] T. Mikó, P. Barkoczy, Determination of the onset of the dynamic recrystallization of a 7075 Al alloy, *Mater. Sci. Forum* 752 (2013) 105–114, [10.4028/www.scientific.net/MSF.752.105](https://doi.org/10.4028/www.scientific.net/MSF.752.105).
- [41] Z.-C. Sun, L.-S. Zheng, H. Yang, Softening mechanism and microstructure evolution of as-extruded 7075 aluminum alloy during hot deformation, *Mater. Char.* 90 (2014) 71–80, <https://doi.org/10.1016/j.matchar.2014.01.019>.
- [42] Z.C. Sun, J.L. Yin, H. Yang, Microstructure evolution and microhardness of 7075 aluminum alloy during heat treatment by considering hot deformation history, *Adv. Mater. Res.* 699 (2013) 851–858, [10.4028/www.scientific.net/AMR.699.851](https://doi.org/10.4028/www.scientific.net/AMR.699.851).
- [43] X. Yang, H. Miura, T. Sakai, Continuous dynamic recrystallization in a superplastic 7075 aluminum alloy, *Mater. Trans.* 43 (2002) 2400–2407, <https://doi.org/10.2320/matertrans.43.2400>.
- [44] T. Rahmaan, P. Zhou, C. Butcher, M.J. Worswick, Strain rate and thermal softening effects in shear testing of AA7075-T6 sheet, *EPJ Web Conf.* 183 (2018), <https://doi.org/10.1051/epjconf/201818302037>, 02037.
- [45] M. Rajamuthamilselvan, S. Ramanathan, Hot deformation behaviour of 7075 alloy, *J. Alloys Compd.* 509 (2011) 948–952, <https://doi.org/10.1016/j.jallcom.2010.09.139>.
- [46] C.J.T. Mason, P.G. Allison, O.L. Rodriguez, D.Z. Avery, B.J. Phillips, C. Leah, Z. McClelland, T.W. Rushing, L. Garcia, J.B. Jordon, Plasticity-damage modeling of strain rate and temperature dependence of aluminum alloy 7075-t651, *J. Dyn. Behav. Mater.* 5 (2019) 105–114, <https://doi.org/10.1007/s40870-019-00188-w>.
- [47] M. Taheri-Mandarjani, A. Zarei-Hanzaki, H.R. Abedi, Hot ductility behavior of an extruded 7075 aluminum alloy, *Mater. Sci. Eng., A* 637 (2015) 107–122, <https://doi.org/10.1016/j.msea.2015.03.038>.
- [48] Z.C. Sun, J.H. Wang, Y. Wang, H. Yang, Hot deformation behavior and fracture of as-extruded 7075 aluminum alloy, *Adv. Mater. Res.* 291–294 (2011) 1051–1056, [10.4028/www.scientific.net/AMR.291-294.1051](https://doi.org/10.4028/www.scientific.net/AMR.291-294.1051).
- [49] J. Lu, Y. Song, L. Hua, K. Zheng, D. Dai, Thermal deformation behavior and processing maps of 7075 aluminum alloy sheet based on isothermal uniaxial tensile tests, *J. Alloys Compd.* 767 (2018) 856–869, <https://doi.org/10.1016/j.jallcom.2018.07.173>.
- [50] D.-N. Zhang, Q.-Q. Shanguan, C.-J. Xie, F. Liu, A modified Johnson–Cook model of dynamic tensile behaviors for 7075-T6 aluminum alloy, *J. Alloys Compd.* 619 (2015) 186–194, <https://doi.org/10.1016/j.jallcom.2014.09.002>.
- [51] M.-Y. Lee, S.-M. Sohn, C.-Y. Kang, D.-W. Suh, S.-Y. Lee, Effects of pre-treatment conditions on warm hydroformability of 7075 aluminum tubes, *J. Mater. Process. Technol.* 155–156 (2004) 1337–1343, <https://doi.org/10.1016/j.jmatprotec.2004.04.200>.
- [52] K. Senthil, M.A. Iqbal, P.S. Chandel, N. Gupta, Study of the constitutive behavior of 7075-T651 aluminum alloy, *Int. J. Impact Eng.* 108 (2017) 171–190, <https://doi.org/10.1016/j.ijimpeng.2017.05.002>.
- [53] K. Huang, R.E. Logé, A review of dynamic recrystallization phenomena in metallic materials, *Mater. Des.* 111 (2016) 548–574, <https://doi.org/10.1016/j.matdes.2016.09.012>.
- [54] J.R. Pothnis, Y. Perla, H. Arya, N.K. Naik, High strain rate tensile behavior of aluminum alloy 7075 T651 and IS 2062 mild steel, *J. Eng. Mater. Technol.* 133 (2011) 1–9, <https://doi.org/10.1115/1.4003113>.
- [55] (n.d. Alumeeco. <https://www.alumeeco.se>. (Accessed 26 October 2020).
- [56] J.I. Goldstein, D.E. Newbury, J.R. Michael, N.W.M. Ritchie, J.H.J. Scott, D.C. Joy, Scanning Electron Microscopy and X-Ray Microanalysis, fourth ed., Springer New York, New York, NY, 2018 <https://doi.org/10.1007/978-1-4939-6676-9>.
- [57] M. Gao, C.R. Feng, R.P. Wei, An analytical electron microscopy study of constituent particles in commercial 7075-T6 and 2024-T3 alloys, *Metall. Mater. Trans., A* 29 (1998) 1145–1151, <https://doi.org/10.1007/s11661-998-0240-9>.
- [58] P.-X. Zhang, H. Yan, W. Liu, X.-L. Zou, B.-B. Tang, Effect of T6 heat treatment on microstructure and hardness of nanosized Al₂O₃ reinforced 7075 aluminum matrix composites, *Metals (Basel)* 9 (2019) 44, <https://doi.org/10.3390/met9010044>.
- [59] M.R. Rokni, A. Zarei-Hanzaki, H.R. Abedi, Microstructure evolution and mechanical properties of back extruded 7075 aluminum alloy at elevated temperatures, *Mater. Sci. Eng., A* 532 (2012) 593–600, <https://doi.org/10.1016/j.msea.2011.11.020>.
- [60] S.F. Cogan, F.W. Gayle, J.D. Klein, F.H. Cocks, M.L. Shepard, Extraction and X-ray analysis of phases in aluminum alloys, *J. Mater. Sci.* 13 (1978) 2687–2691, <https://doi.org/10.1007/BF02402756>.
- [61] S.I. Wright, M.M. Nowell, D.P. Field, A review of strain analysis using electron backscatter diffraction, *Microsc. Microanal.* 17 (2011) 316–329, <https://doi.org/10.1017/S1431927611000055>.
- [62] S. Gourdet, F. Montheillet, An experimental study of the recrystallization mechanism during hot deformation of aluminium, *Mater. Sci. Eng., A* 283 (2000) 274–288, [https://doi.org/10.1016/S0921-5093\(00\)00733-4](https://doi.org/10.1016/S0921-5093(00)00733-4).
- [63] S. Gourdet, F. Montheillet, A model of continuous dynamic recrystallization, *Acta Mater.* 51 (2003) 2685–2699, [https://doi.org/10.1016/S1359-6454\(03\)00078-8](https://doi.org/10.1016/S1359-6454(03)00078-8).
- [64] R.D. Doherty, D.A. Hughes, F.J. Humphreys, J.J. Jonas, D.J. Jensen, M.E. Kassner, W.E. King, T.R. McNelley, H.J. McQueen, A.D. Rollett, Current issues in recrystallization: a review, *Mater. Sci. Eng., A* 238 (1997) 219–274, [https://doi.org/10.1016/S0921-5093\(97\)00424-3](https://doi.org/10.1016/S0921-5093(97)00424-3).
- [65] B. Tang, L. Xiang, L. Cheng, D. Liu, H. Kou, J. Li, the formation and evolution of shear bands in plane strain compressed nickel-base superalloy, *Metals (Basel)* 8 (2018) 141, <https://doi.org/10.3390/met8020141>.
- [66] T. Kiriya, Numerical study of shear band formation in triaxial compression tests, *J. Jpn. Soc. Civ. Eng. Ser A2 (Applied Mech.)* (2014), <https://doi.org/10.2208/jscejam.70.1>.
- [67] M. Al-Chalabi, F.J. McCormick, C.L. Huang, Strain distribution within compressed circular cylinders, *Exp. Mech.* 14 (1974) 497–501, <https://doi.org/10.1007/BF02323151>.
- [68] M. Sanjari, P. Saidi, A. Karimi Taheri, M. Hossein-Zadeh, Determination of strain field and heterogeneity in radial forging of tube using finite element method and microhardness test, *Mater. Des.* 38 (2012) 147–153, <https://doi.org/10.1016/j.matdes.2012.01.048>.